RECEIVED
22 February 2026

REVISED
29 March 2026

ACCEPTED
20 April 2026

PAPER

Viscosity Rise of Supercritical Liquid Copper Above the Frenkel Line and Related Structural Features: A Molecular Dynamics and Topological Data Analysis Study

F. Ferracina[1,2,*], A.K.A. Lu[3,4], X.N. Du[5], N. Chen[5], M.I. Ojovan[6], H. Suito[1,2], D. V. Louzguine-Luzgin[2]

[1]Mathematical Science Center for Co-creative Society, Tohoku University, Sendai 980-8577, Japan [2]Advanced Institute for Materials Research (WPI-AIMR), Tohoku University, Sendai 980-8577, Japan [3]Department of Materials Engineering, The University of Tokyo, Tokyo 113-8656, Japan [4]Research Center for Materials Nanoarchitectonics (MANA), National Institute for Materials Science (NIMS), Tsukuba 305-0044, Japan [5]Key Laboratory for Advanced Materials (MOE), School of Materials Science and Engineering, Tsinghua University, Beijing 100084, China [6]School of Chemical, Materials and Biological Engineering, The University of Sheffield, Sheffield S1 3JD, UK

*Author to whom any correspondence should be addressed.

E-mail: fabiana@tohoku.ac.jp

Keywords: viscosity, supercritical liquid copper, Frenkel line, molecular dynamics, topological data analysis, persistent homology

Abstract

We present a comprehensive molecular dynamics (MD) and topological data analysis (TDA) study of liquid copper structure and transport properties at supercritical pressure. Contrary to expectations that viscosity decreases monotonically with temperature approaching 10^{-5} Pas [Angell, 1995], we observe an unusual viscosity increase at high temperatures. This behavior correlates with fundamental changes in local atomic topology and medium-range order. Using persistent homology (PH) to characterize 1-dimensional holes (H_1) and 2-dimensional voids (H_2), combined with pair and radial distribution functions (PDFs, RDFs) and coordination number analysis, we reveal significant structural reorganization between 5000 K and 10000 K at 100 kbar (10 GPa). Shannon entropy increases by 14–15% for both H_1 and H_2 features above the Frenkel line, indicating a transition from the liquid-like to gas-like dynamics while maintaining high interatomic coordination. Our results demonstrate that this transition represents a genuine transition in both transport properties and topological structure in supercritical metallic liquids.

1 Introduction

Transport properties of liquids at extreme pressures and temperatures govern fundamental processes in condensed matter physics, geophysics, and materials science. While viscosity of conventional liquids decreases with temperature [Landau and Lifshitz, 1964], behavior under supercritical conditions at high temperature remains not completely understood and may deviate from classical predictions. Achieving a supercritical liquid state suppresses boiling, which can hardly be avoided at ambient pressure, and enables investigation of the high-temperature regime of the temperature dependence of viscosity [Angell, 1995].

Recent studies suggest that supercritical liquids exhibit a thermodynamic transition, [Trachenko, 2023, Ojovan and Louzguine-Luzgin, 2024a] associated with the Frenkel line (FL) [MacDougall, 1947, Simeoni et al., 2010], a boundary separating solid-like and gas-like regimes, mostly explored using specific heat capacity. Below the FL, particles oscillate around quasi-equilibrium positions before diffusing, maintaining transverse phonon modes. Above the FL, particles move ballistically without oscillatory motion [Brazhkin et al., 2012a,b]. This transition manifests itself in thermodynamic properties including specific heat, thermal conductivity [Bolmatov et al., 2013, 2015], and collective vibrations [Bolmatov et al., 2014, Larini et al., 2008].

While the FL has been explored in noble gases and molecular liquids, metallic liquids remain underexplored [Wax and Mocchetti, 2023, Ojovan and Louzguine-Luzgin, 2024b]. Here, we study the behavior of a supercritical liquid copper at 100 kbar (10 GPa) using MD simulations. Interestingly, we find an anomalous positive temperature dependence of viscosity at high temperature, contrary to classical predictions [Angell, 1995, Louzguine-Luzgin et al., 2016]. To

examine this behavior, we combine conventional structural analysis with persistent homology [Edelsbrunner and Harer, 2010, Carlsson, 2009], which captures multi-scale topological features (loops and voids that persist across different length scales) providing insights into medium-range order not apparent from pair correlations alone.

2 Methods

2.1 Molecular Dynamics Simulations

We performed classical MD simulation procedures using LAMMPS (Large-scale Atomic/Molecular Massively Parallel Simulator) [Plimpton, 1995] with graphics processing unit (GPU) acceleration [Brown et al., 2011]. An embedded-atom method (EAM) potential for Cu developed by Mendelev and King [Mendelev and King, 2013] was employed, chosen for its accurate reproduction of thermodynamic and structural properties in both liquid and solid phases; EAM-based MD has been similarly applied to characterize the structural and mechanical properties of metallic glass matrix composites [Bogtob et al., 2024]. Simulations were carried out in the NPT ensemble using the Nosé-Hoover thermostat [Nosé, 1984, Hoover, 1985] and a barostat [Berendsen et al., 1984, Martyna et al., 1994] under periodic boundary conditions with a time step of 1 fs.

Initial configurations were prepared by equilibrating systems containing 500,000 atoms in a cubic simulation box with periodic boundary conditions to minimize finite-size effects (Figure S1). The initial atomic configuration was an FCC Cu crystal with lattice parameter $a = 3.615$ Å, yielding a cubic box of approximately 18 nm side length at ambient density. Prior to equilibration, a standard LAMMPS energy minimization procedure (conjugate gradient algorithm, force tolerance 10^{-6} eV/Å) was applied to each initial configuration to remove any unphysical atomic overlaps possibly introduced during construction.

A supercritical pressure of $P = 100$ kbar (10 GPa), estimated from thermodynamic considerations [Zinoviev, 1989, Demin et al., 2019], was applied at temperatures ranging from 2000 K to 12000 K in 1000 K increments. This range was chosen to span the expected location of the Frenkel line for Cu at 10 GPa (∼8000 K), capturing both the liquid-like regime below and the gas-like regime above, while remaining within the stability range of the employed EAM potential.

Each simulation consisted of an initial equilibration phase of 100 ps before data collection over an additional 100 ps. At high temperatures (≥4000 K), 100 ps was sufficient for full thermodynamic equilibration, as confirmed by stability of energy and density. At lower temperatures, longer runs were required: 300 ps equilibration was used at 3000 K, and up to 1.2 ns at 2000 K to obtain stable viscosity values. The liquid relaxation time was estimated from the variations in energy and density as functions of time. Additionally, longer simulation time of 1 ns was used for simulation at 1000-1600 K under ambient pressure. The time step was set to 1 fs to ensure accurate integration of the equations of motion. Atomic trajectories were saved every 100 time steps (0.1 ps) for subsequent structural analysis.

2.2 Transport Property Calculations

Viscosity was computed using the Green-Kubo formalism [Green, 1954, Kubo, 1957]:

$$\eta = \frac{V}{k_B T} \int_0^\infty \langle P_{\alpha\beta}(t) P_{\alpha\beta}(0) \rangle \, dt \tag{1}$$

where V is the system volume, k_B is Boltzmann's constant, T is temperature, and $P_{\alpha\beta}$ is the off-diagonal pressure tensor component. Each viscosity value represents the average of at least 10 independent calculations with 95% confidence intervals.

The diffusion coefficient (D) was calculated from the mean squared displacement (MSD) via the Einstein relation:

$$D_s = \frac{1}{2s} \lim_{t\to\infty} \frac{d}{dt} \langle |\mathbf{r}(t) - \mathbf{r}(0)|^2 \rangle \tag{2}$$

where s is the spatial dimensionality.

2.3 Structural Analysis

Pair distribution functions (PDFs, $g(r)$), radial distribution functions (RDFs), and coordination numbers (CNs) were calculated using standard methods. The RDF was calculated as:

$$\mathrm{RDF}(r) = 4\pi r^2 N_D \cdot g(r) \tag{3}$$

where $N_D = 500{,}000/V$ is the average atomic number density. Coordination numbers were obtained by integrating the RDF to the first minimum:

$$\mathrm{CN}(r) = 4\pi N_D \int_0^{r_{\min}} g(r) r^2 \, dr \tag{4}$$

2.4 Topological Data Analysis

Persistent homology analysis quantified topological features using Alpha complex filtration [Edelsbrunner and Mücke, 1994] via HomCloud [Obayashi et al., 2022]. Unlike the Vietoris-Rips complex based purely on pairwise distances, the Alpha complex derives from Delaunay triangulation and captures the topology of the union of growing atomic balls restricted to the Voronoi diagram. This approach offers three advantages for dense atomic systems: (i) geometric fidelity avoiding topological noise from high-dimensional artifacts; (ii) computational efficiency with fewer simplices enabling analysis of 500,000 atoms; and (iii) direct physical interpretation where the filtration parameter corresponds to atomic probe radius.

Following Nakamura et al. [2015], birth scale b_k indicates the maximum neighboring distance for a hole c_k, death scale d_k indicates hole size, and life scale $d_k - b_k$ represents feature robustness. Features far from the diagonal in persistence space have long life scales and represent genuine structural characteristics rather than noise [Buchet et al., 2016]. The Alpha complex naturally handles cases where particles maintain high coordination, while medium-range connectivity changes through explicit spatial embedding.

For each configuration, we computed persistence diagrams for: β_0 (connected components), β_1 (1D holes/loops, H_1), and β_2 (2D voids/cavities, H_2). Each feature appears as a point (b, d) where b is the birth scale and d is the death scale. From persistence diagrams, we extracted the Shannon entropy, which measures the diversity and distribution of topological features. That is,

$$S = -\sum_i p_i \log p_i \tag{5}$$

where $p_i = (d_i - b_i)/P_k$ is normalized persistence (P_k is total persistence), and weighted mean persistence:

$$\bar{P}_k^w = \frac{\sum_i f_i (d_i - b_i)}{\sum_i f_i} \tag{6}$$

where f_i is feature frequency.

Statistical significance was assessed using Mann-Whitney U and Kolmogorov-Smirnov tests with Bonferroni correction ($\alpha = 0.0167$). Bootstrap confidence intervals (95%, 1000 iterations) ensured robustness. Correlations between TDA metrics and viscosity were assessed using Spearman rank correlation, preferred over Pearson's r given the non-monotonic viscosity behaviour at the Frenkel line minimum; split-sample correlations were computed separately for temperatures below and above the Frenkel line. Effect sizes were quantified using Cohen's d with pooled standard deviation.

3 Results

3.1 Transport Properties

The activation energy of the liquid Cu viscosity at ambient pressure (1 bar) was found to be 32 kJ/mol (Figure 1), which is very close to the value of 30.5 kJ/mol reported experimentally [Gale and Totemeier, 2004]. A similar value was found for the supercritical liquid Cu in the range from 2000 to 7000 K (Figure 1). To verify the applicability of the interatomic potential for calculating viscosity, the equilibrium liquid Cu viscosity was compared with the measured values [Assael et al., 2010], and good correspondence was observed. Under the same conditions, the liquid density of 8.028 g/cm^3 at 1400 K is also not far from the experimental value of 7.956 g/cm^3 [Cahill and Kirshenbaum, 1962].

The initial atomic configurations at each temperature used for viscosity measurement were taken from snapshots along a continuous heating trajectory at a rate of 10^{13} K/s, at which Cu melted at approximately 1900 K. The energy and density monitored as functions of time confirmed that stable thermodynamic states were reached within a few picoseconds at 2000 K and above, validating the use of 100 ps production windows at high temperatures. The results also correlate well with the MD simulation results [Demin et al., 2020] using another potential [Mishin et al., 2001].

At the supercritical pressure of 100 kbar, viscosity exhibits remarkable non-monotonic behavior as a function of temperature (Figure 1). Below approximately 8000 K, viscosity decreases with increasing temperature (reaching a minimum at 8000 K (-7.29 ln Pa·s)) following the classical

Arrhenius-like behavior expected for liquids. However, above this temperature, the viscosity begins to increase with a further increase in temperature. This anomalous behavior coincides with the estimated location of the Frenkel line for Cu at 100 kbar based on the thermodynamic criteria [Ojovan and Louzguine-Luzgin, 2024b,a].

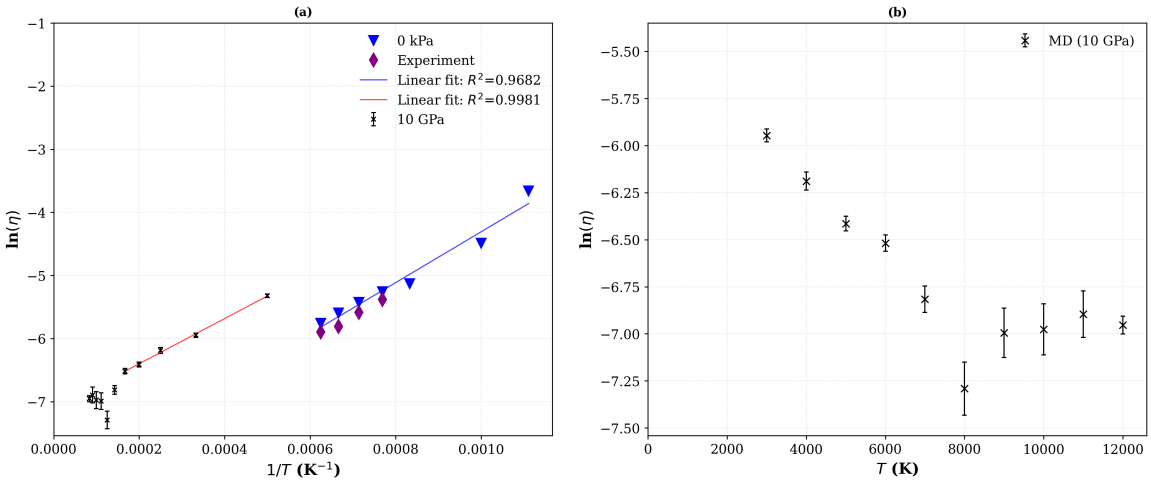

Figure 1. (a) Arrhenius plot comparing ambient pressure (purple triangles), experimental data (orange diamonds), and 10 GPa (black circles). Linear fit ($R^2 = 0.9682$, blue line) shows good agreement at lower temperatures with deviation at high temperature. (b) Temperature dependence at 10 GPa showing minimum near 8000 K.

The diffusion coefficient behaves complementary to viscosity: it increases continuously with temperature but exhibits a distinct change in slope near 7000 K (Figure 2). Below 7000 K, the diffusion coefficient increases gradually with a slope of 0.0004 $\mathrm{m}^2/(\mathrm{s}\cdot\mathrm{K})$ ($R^2 = 0.9998$), characteristic of thermally activated diffusion in a liquid. Above 8000 K, the slope increases to 0.0007 $\mathrm{m}^2/(\mathrm{s}\cdot\mathrm{K})$ ($R^2 = 0.9891$), indicating a transition to more efficient atomic transport. This kink in $\mathrm{d}D/\mathrm{d}T$ and the viscosity minimum provide dynamical evidence for the structural transition.

The product $D\eta/T$, which according to the Stokes-Einstein relation should remain constant for simple liquids, shows a systematic deviation above the Frenkel line, indicating a breakdown of the conventional hydrodynamic description. This decoupling of diffusion and viscosity is a hallmark of the transition from liquid-like collective motion to gas-like ballistic transport.

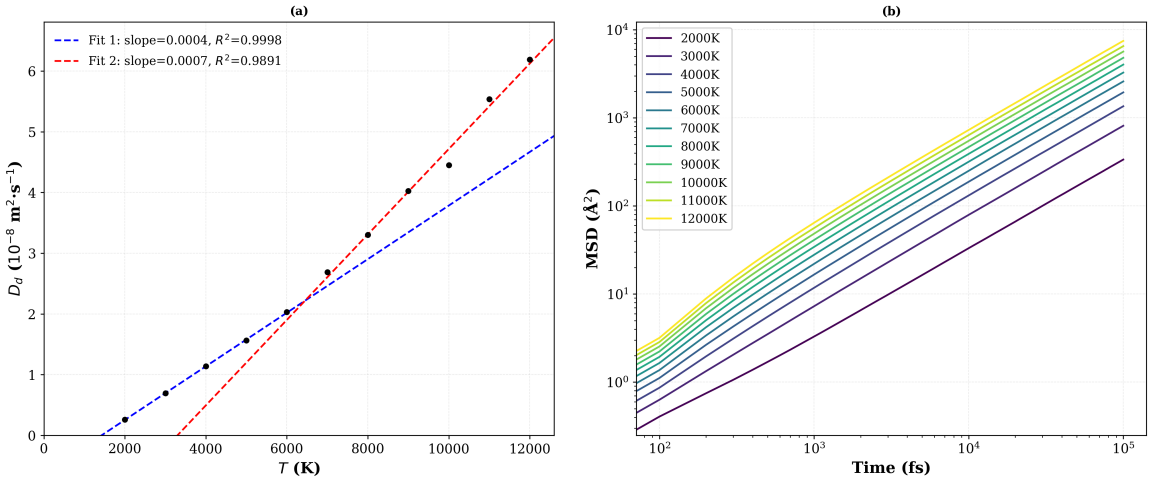

Figure 2. (a) Diffusion coefficient showing slope change near the FL. (b) Mean squared displacement on log-log scale for 2000–12000 K.

To assess the statistical significance of the Stokes–Einstein breakdown, $D\eta/T$ was computed at all simulated temperatures with propagated uncertainties $\sigma_{D\eta/T} = (D\eta/T) \cdot (\sigma_\eta/\eta)$, where σ_η is the 95% confidence interval of the viscosity (Table 1). The deviation above the Frenkel line is statistically significant at all five above-FL temperatures: the confidence intervals do not overlap the below-FL mean at any point. The largest departure occurs at 8000 K, coinciding with the viscosity minimum, where $D\eta/T$ is reduced by 48% relative to the below-FL mean

($\bar{SE}_{\text{below}} = 0.543 \times 10^{-14}$ m^2·Pa·K^{-1}). A positive linear trend in $D\eta/T$ above FL ($p = 0.030$, $R^2 = 0.84$) indicates a systematic recovery toward the liquid-like baseline with increasing temperature, consistent with a gradual crossover rather than a sharp transition.

Table 1. Stokes–Einstein product $D\eta/T$ at all simulated temperatures (10 GPa) with propagated uncertainties. Uncertainty estimated as $\sigma_{D\eta/T} = (D\eta/T) \cdot (\sigma_\eta/\eta)$, where σ_η is the 95% CI on viscosity. The below-FL mean is $\bar{SE} = 0.543 \times 10^{-14}$ m^2·Pa·K^{-1}. All above-FL values differ significantly from $\bar{SE}$ (non-overlapping confidence intervals).

T (K)	D (10^{-8} m^{2}s^{-1})	η (mPa·s)	$D\eta/T$ (10^{-14} m^2·Pa·K^{-1})	Regime
2000	0.262	4.880 ± 0.226	0.639 ± 0.030	Below FL
3000	0.693	2.610 ± 0.045	0.603 ± 0.010	Below FL
4000	1.137	2.050 ± 0.069	0.583 ± 0.020	Below FL
5000	1.564	1.640 ± 0.022	0.513 ± 0.007	Below FL
6000	2.033	1.480 ± 0.030	0.501 ± 0.010	Below FL
7000	2.688	1.100 ± 0.035	0.423 ± 0.013	Below FL
8000	3.301	0.682 ± 0.044	0.281 ± 0.018	Above FL
9000	4.026	0.917 ± 0.056	0.410 ± 0.025	Above FL
10000	4.452	0.934 ± 0.057	0.416 ± 0.025	Above FL
11000	5.538	1.010 ± 0.060	0.509 ± 0.030	Above FL
12000	6.188	0.955 ± 0.031	0.492 ± 0.016	Above FL

3.2 Structural Characterization

The RDF evolves systematically with temperature (Figure 3). At 2000–5000 K, well-defined first and second peaks indicate a significant degree of short and medium-range order. Approaching 8000 K, the first RDF peak decreases and broadens, while the second peak becomes less pronounced, indicating reduced structural correlations.

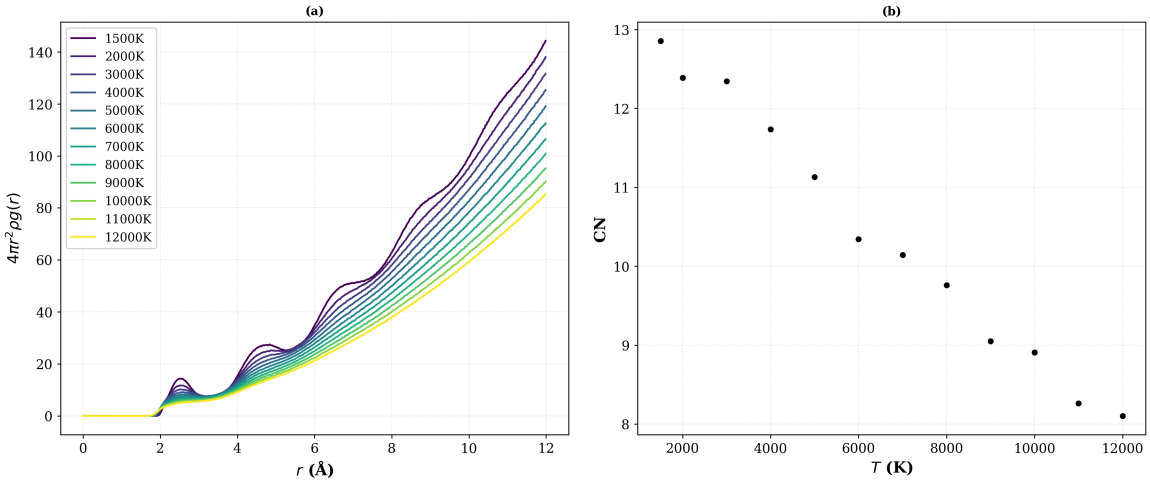

Figure 3. (a) RDF from 1500 K to 12000 K showing systematic broadening. (b) Coordination number decreases from 12.8 at 1500 K to 8.3 at 12000 K.

The coordination number decreases gradually with temperature without a pronounced kink (Figure 3b). From 5000 K to 10000 K, it decreases from 11.1 to 8.9 (20% reduction). This maintenance of high coordination despite gas-like dynamics suggests the FL transition involves genuine topological reorganization rather than simple dilution [Chang et al., 2022].

The broadening of the RDF second peak in reciprocal space manifests itself as changes in the principal peak (Q_2) of the structure factor $S(Q)$. As shown by Onodera et al. [2019], the principal peak reflects orientational correlations of local structural motifs, while the first sharp diffraction peak (Q_1) indicates intermediate-range periodicity. In metallic liquids, the principal peak dominates the low-Q region. The evolution of the RDF across the FL corresponds to *changes* in the position and width of Q_2, reflecting the weakening of the packing efficiency in the medium-range. Persistent homology reveals structural features "hidden in the halo pattern" not apparent from $S(Q)$ or $g(r)$ alone [Onodera et al., 2019], with the proliferation of diverse H_1 and H_2 features above the FL providing direct geometric evidence for structural heterogeneity.

3.3 Topological Data Analysis

3.3.1 1-dimensional Homology (H_1) The persistence diagrams for H_1 features show a significant evolution between 5000 K and 10000 K (Figure 4). At 5000 K, 733 distinct topological features occur with total frequency 1.86×10^6, indicating repeated loop structures. At 10000 K, the features increase to 1,651 (+125%) while the total frequency decreases to 1.57×10^6 (−15%), reflecting greater diversity and reduced individual stability.

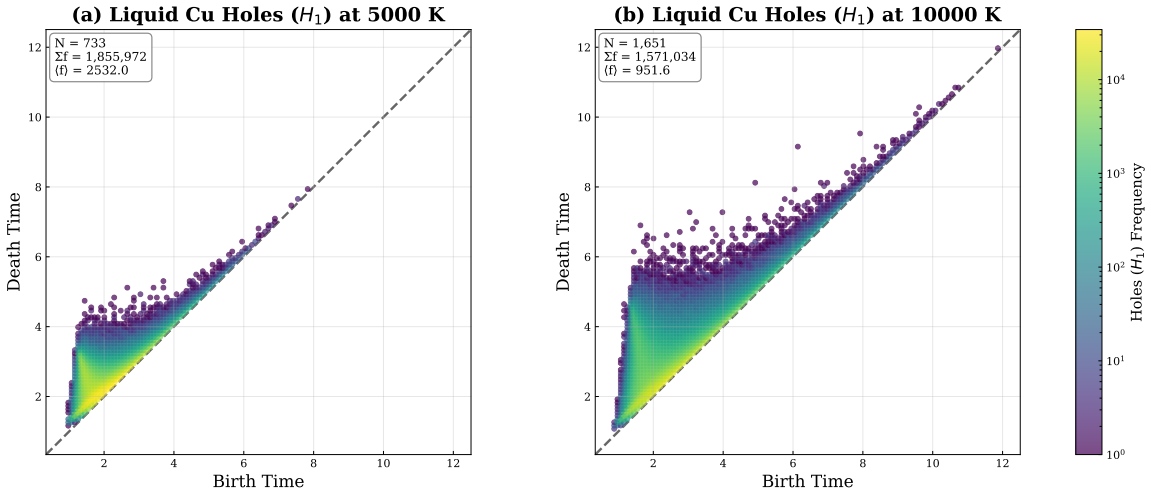

Figure 4. Persistence diagrams for H_1 features at (a) 5000 K and (b) 10000 K. Points colored by logarithmic frequency. Increased features (733 to 1,651) with decreased frequency indicates structural diversification.

A binned analysis with bootstrap confidence intervals reveals a detailed reorganization (Figure S2). Short-persistence features ([0.00, 1.05) Å) show similar frequencies at both temperatures, dominated by transient loops. At intermediate and high persistence ([2.10, 3.15) Å and above), 10000 K shows dramatic emergence of spatially extended but less frequent features, evidencing a transition to larger-scale topological heterogeneity.

Statistical metrics show consistent trends (Figure S3). Shannon entropy increases from 5.07 [4.97, 5.18] at 5000 K to 5.79 [5.72, 5.86] at 10000 K (+14.2%, non-overlapping CI), quantifying increased diversity. The frequency-weighted mean persistence increases from 0.408 [0.363, 0.466] Å to 0.481 [0.438, 0.531] Å (+17.9%), demonstrating that emergent structures are more diverse and spatially extended. The prominent structures (frequency >Q3) increase from 183 to 413 (+126%), consistent with a transition from dominant cage structures to diverse transient configurations.

The spatial evolution in the birth-death space (Figure 5) shows a net loss of high-frequency, short-persistence features (loss: 876,627) and the emergence of lower-frequency, longer-persistence features (gain: 589,645), yielding net change of $-286,982$ with the gain/loss ratio 0.67. This pattern indicates a transition from structured liquid with characteristic cages to heterogeneous supercritical fluid.

3.3.2 2-dimensional Homology (H_2) The H_2 features show parallel but more pronounced trends (Figure 6). At 5000 K, 1,296 distinct features occur with frequency 9.49×10^5; at 10000 K, features increase to 2,838 (+119%) with frequency 7.30×10^5 (−23%).

The binned analysis (Figure S5) reveals a similar reorganization, with short-persistence voids showing high frequencies at both temperatures while medium and long-persistence voids emerge at 10000 K, confirming spatially extended but transient structures in the supercritical regime.

Statistical comparison (Figure S6) shows Shannon entropy increasing from 4.98 [4.86, 5.15] to 5.72 [5.62, 5.83] (+14.7%), while weighted mean persistence increases from 0.274 [0.240, 0.324] Å to 0.330 [0.300, 0.371] Å (+20.4%). All metrics show non-overlapping confidence intervals. Void topology changes are more pronounced than holes, directly correlating with collisional viscosity enhancement where atoms maintain dense packing without stable medium-range cage connectivity.

The difference map (Figure 7) shows net frequency loss of $-814,614$ (stable cages) combined with gain of 465,096 (diverse voids), yielding net change of $-349,428$ with gain/loss ratio 0.57, more pronounced than for holes.

Tables 2 and 3 summarize key topological metrics with bootstrap confidence intervals, confirming the topological transition at ∼8000 K.

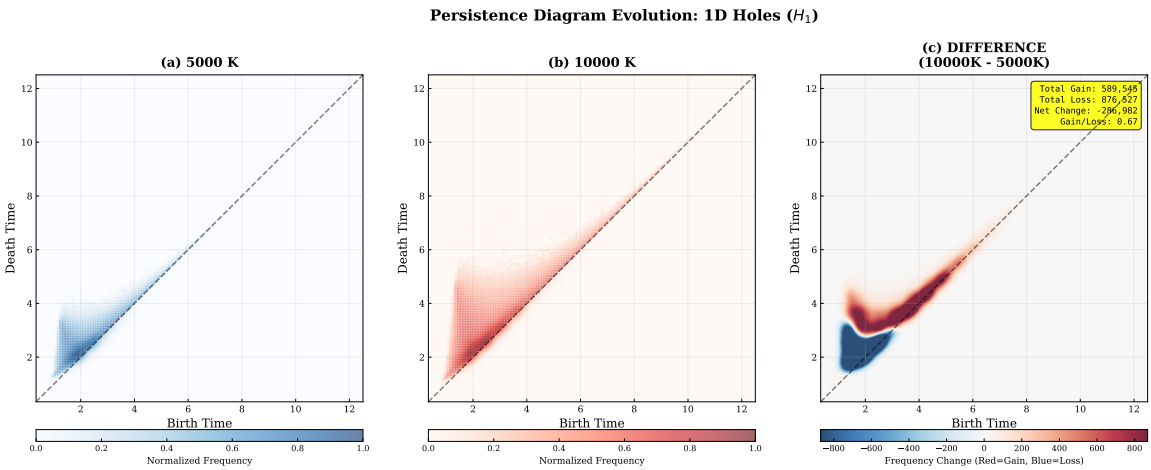

Figure 5. Spatial evolution of H_1 features. (a) 5000 K persistence diagram. (b) 10000 K persistence diagram. (c) Difference map showing frequency loss (blue) and gain (red).

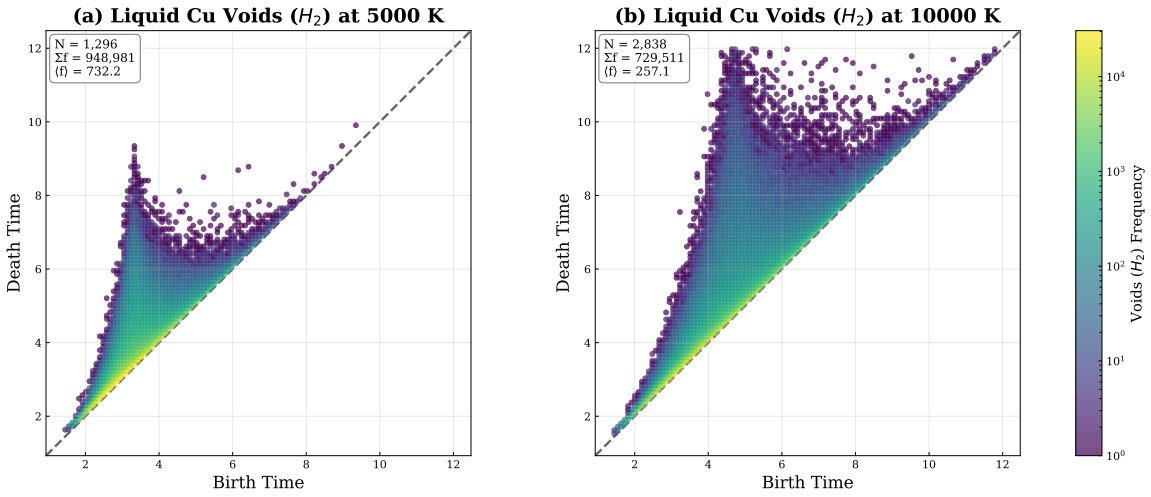

Figure 6. Persistence diagrams for H_2 features at (a) 5000 K and (b) 10000 K. Increased feature count (+119%) with decreased frequency (−23%) indicates diverse void structures with reduced stability.

3.3.3 Extensivity Analysis For bulk systems, Betti numbers β_n and related quantities should scale with the system size. Nakamura et al. [2015] demonstrated that for large monatomic systems, the peak Betti numbers are proportional to the atom number N, a property termed "extensivity." Following their framework, normalized distributions can be defined:

$$\rho_n(b,d) = \frac{4\pi}{3N} \sum_{k \in D^n} f_k \delta(b - b_k) \delta(d - d_k) \tag{7}$$

For our $N = 500{,}000$ system, the extensivity term indicates that the observed changes reflect genuine structural differences per-atom rather than finite-size effects. The dramatic increase in total H_1 features (+125%) with decreased frequency indicates a fundamental change in the topological motif distribution across the FL, consistent with a transition in the underlying potential energy landscape from few deep basins (characteristic cages) to a rugged landscape with many shallow basins (diverse transient configurations) [Nakamura et al., 2015].

Table 2. Summary of H_1 metrics with 95% bootstrap CI.

H_1 **Metric**	**5000 K**	**10000 K**	**% Change**
Total Features	733	1,651	+125.2%
Total Frequency	1.86×10^6	1.57×10^6	−15.4%
Shannon Entropy	5.07 [4.97, 5.18]	5.79 [5.72, 5.86]	+14.2%
Weighted Persistence (Å)	0.408 [0.363, 0.466]	0.481 [0.438, 0.531]	+17.9%

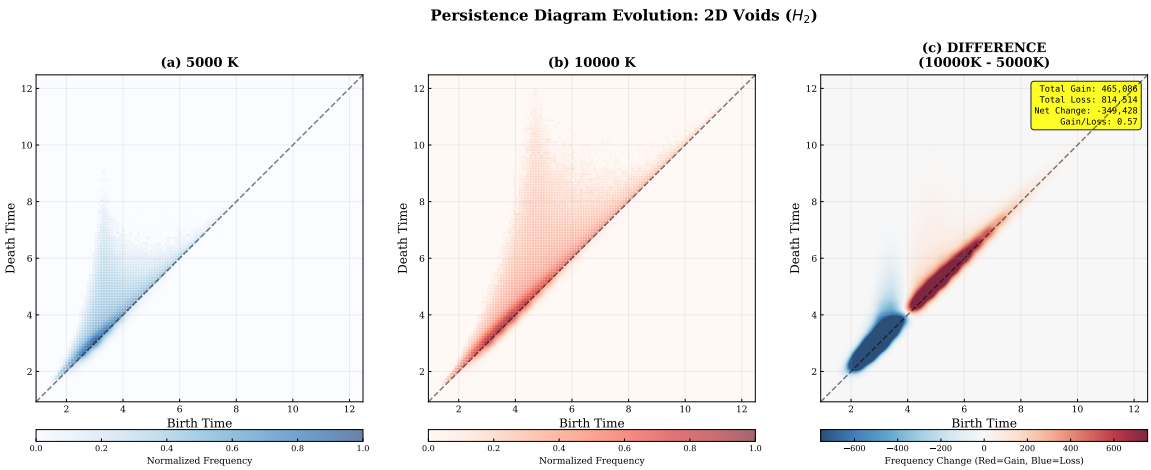

Figure 7. Spatial evolution of H_2 features. (a) 5000 K persistence diagram. (b) 10000 K persistence diagram. (c) Difference map.

Table 3. Summary of H_2 metrics with 95% bootstrap CI.

H_2 **Metric**	**5000 K**	**10000 K**	**% Change**
Total Features	1,296	2,838	+119.0%
Total Frequency	9.49×10^5	7.30×10^5	−23.1%
Shannon Entropy	4.98 [4.86, 5.15]	5.72 [5.62, 5.83]	+14.7%
Weighted Persistence (Å)	0.274 [0.240, 0.324]	0.330 [0.300, 0.371]	+20.4%

3.3.4 Statistical Validation Rigorous hypothesis testing confirms topological transitions (Figures S4 and S7). For H_1, persistence distributions differ significantly (Kolmogorov-Smirnov: $D = 0.1711$, $p = 1.89 \times 10^{-13}$), with mean persistence increasing from 0.911 to 1.354 (+49%). The frequency distributions show substantial shift towards low-frequency features at 10000 K (Mann-Whitney U: $p = 3.61 \times 10^{-5}$). For H_2, mean persistence increases from 1.548 to 2.191 (+42%), with highly significant distribution differences ($p = 2.57 \times 10^{-19}$ for K-S, $p = 6.87 \times 10^{-12}$ for M-W).

All tests with Bonferroni correction ($\alpha = 0.0167$) show highly significant differences ($p < 10^{-5}$, Table 4), confirming a genuine structural transition at the FL.

3.3.5 Temperature-Resolved Topological Analysis To confirm that the structural trends identified at 5000 K and 10000 K are representative of the broader temperature evolution, we extended the persistent homology analysis across all simulated temperatures (2000–12000 K). Figure 8 summarizes the key metrics.

Shannon entropy increases monotonically with temperature for H_1 loop features (Figure 8a), confirming that the 5000 K and 10000 K values bracket a smooth, continuous topological evolution. H_2 void entropy follows the same trend on average but exhibits localised non-monotonicities at 6000 K and 11000 K, where a simultaneous reduction in feature count and increase in weighted persistence indicates periodic reorganisation of the void network between a proliferation state (many small, transient voids) and a consolidation state (fewer but spatially larger voids). This behaviour is unique to 3D void topology and absent in H_1, suggesting it reflects a characteristic of cage-like structures rather than general topological disorder.

The topology–transport relationship was quantified using Spearman rank correlation between H_1 Shannon entropy and $\ln \eta$ across all 11 temperature points ($\rho = -0.827$, $p = 0.002$). Split-sample analysis at the Frenkel line reveals a sign reversal: below 8000 K, $\rho = -1.000$

Table 4. Statistical significance tests with Bonferroni correction ($\alpha = 0.0167$).

Feature	**Test**	**Statistic**	**p-value**
H_1	M-W U (frequency)	—	3.61×10^{-5}
H_1	M-W U (persistence)	—	5.58×10^{-19}
H_1	K-S	$D = 0.1711$	1.89×10^{-13}
H_2	M-W U (frequency)	—	6.87×10^{-12}
H_2	M-W U (persistence)	—	2.83×10^{-23}
H_2	K-S	$D = 0.1558$	2.57×10^{-19}

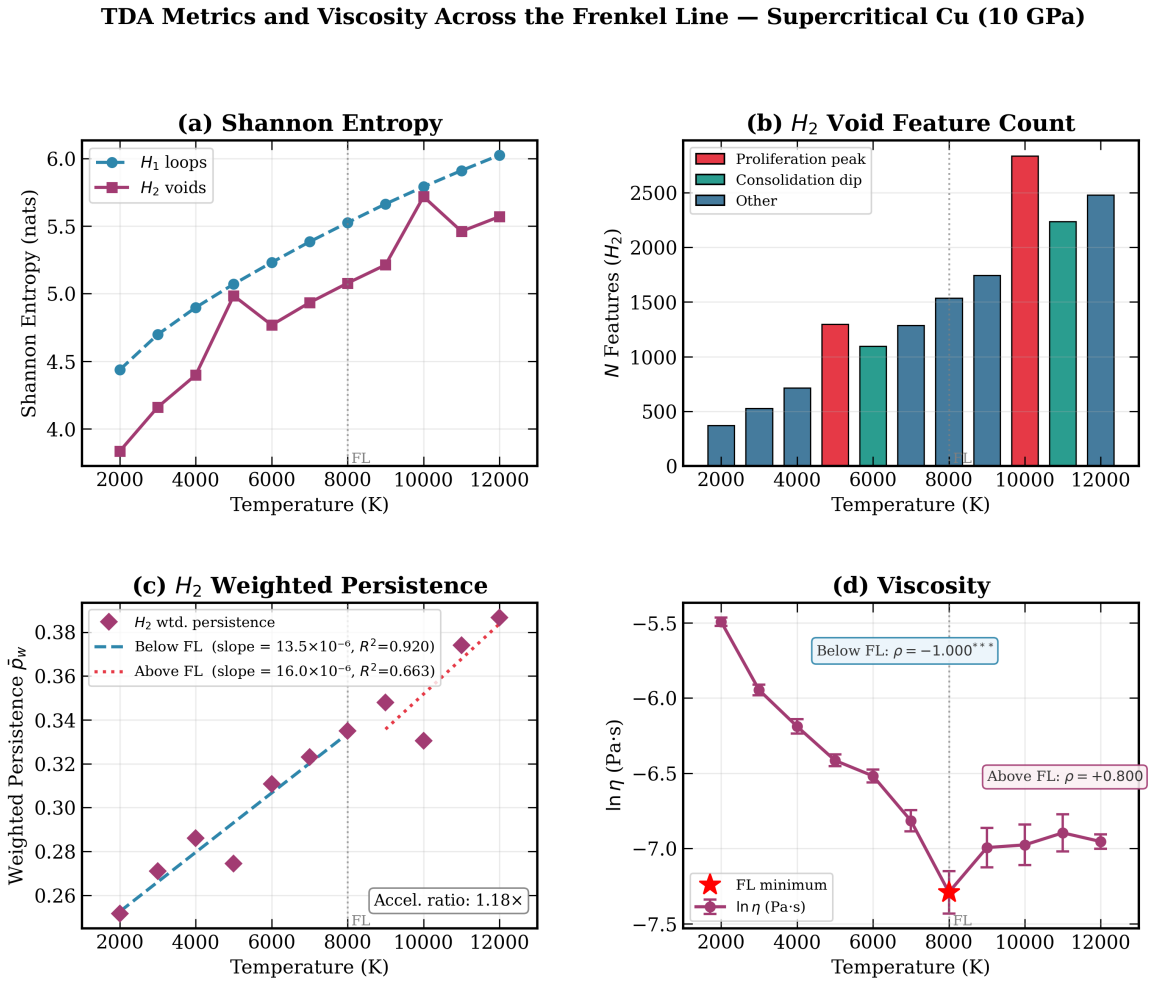

Figure 8. Topological data analysis metrics and viscosity of supercritical Cu across the Frenkel line (10 GPa, 2000–12000 K). The dotted vertical line marks the Frenkel line at ∼8000 K. (a) Shannon entropy for H_1 loops and H_2 voids; H_2 exhibits non-monotonic behaviour absent in H_1. (b) H_2 void feature count showing alternating proliferation peaks (red, 5000 K and 10000 K) and consolidation dips (teal, 6000 K and 11000 K). (c) H_2 weighted persistence with piecewise linear fits; the slope accelerates by a factor of 1.18 above the Frenkel line.(d) Viscosity $\ln \eta$ with 95% confidence intervals. Spearman rank correlations between H_1 Shannon entropy and $\ln \eta$ reverse sign across the Frenkel line ($\rho = -1.000$, $p < 0.001$ below; $\rho = +0.800$ above), reflecting a fundamental change in the topology–transport relationship.

($p < 0.001$, $n = 7$), consistent with the conventional liquid picture in which structural disorder facilitates flow; above 8000 K, $\rho = +0.800$ ($n = 4$), indicating that further topological diversification is associated with increased viscosity in the gas-like regime. The entropy jump at the Frenkel line is quantitatively large, with Cohen's $d = 2.76$ for H_1 and $d = 2.45$ for H_2, confirming that the topological transition identified in the two-temperature comparison is well-separated from thermal noise across the full temperature range. H_2 weighted persistence additionally shows a 1.18-fold acceleration in its rate of increase above the Frenkel line ($R^2 = 0.92$ below, $R^2 = 0.66$ above; Figure 8c), consistent with the emergence of larger void structures in the gas-like regime.

3.3.6 Comparison to Crystalline and Glassy Systems The persistence distributions were compared to qualitative reference ranges for crystalline structures (Figures 9 and 10). At 5000 K, the liquid exhibits topological signatures intermediate between crystalline and highly disordered structures. At 10000 K, the signatures shift toward more disordered configurations, consistent with the gas-like nature above the Frenkel line, though still maintaining significantly more structure than a true ideal gas. The death time distribution (middle) peak shifts from ∼6 (5000 K) to ∼8 (10000 K), reflecting increased characteristic length scales. The summary table (right) quantifies all key metrics: mean persistence increases from 0.829 to 1.271 (+53.4%), Shannon entropy from 5.206 to 5.860 (+12.6%), and compactness from 0.431 to 0.558 (+29.5%). The hole topology at both temperatures shows an intermediate character between the BCC and FCC crystalline references, with 10000 K trending toward more disordered, heterogeneous configurations.

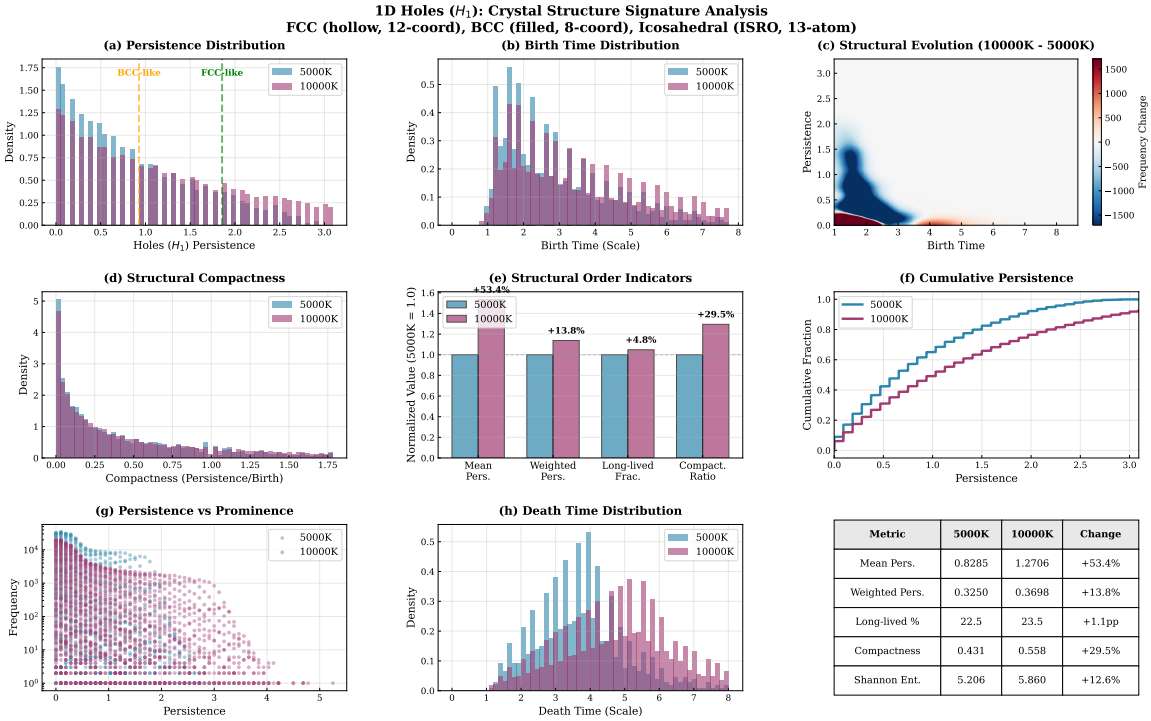

Metric	5000K	10000K	Change
Mean Pers.	0.8285	1.2706	+53.4%
Weighted Pers.	0.3250	0.3698	+13.8%
Long-lived %	22.5	23.5	+1.1pp
Compactness	0.431	0.558	+29.5%
Shannon Ent.	5.206	5.860	+12.6%

Figure 9. Topological signatures of H_1 features (1D holes) in liquid Cu at 5000 K and 10000 K compared to the crystalline structure references (FCC, BCC, icosahedral). (a) Persistence distribution with reference lines for the BCC-like and FCC-like structures. (b) Birth time distribution. (c) Structural evolution showing frequency change between temperatures. (d) Structural compactness quantified by the persistence/birth ratio. (e) Normalized structural order indicators showing percent changes in mean persistence (+53.4%), weighted persistence (+13.8%), long-lived feature fraction (+1.1pp), compactness (+29.5%), and Shannon entropy (+12.6%). (f) Cumulative persistence distributions. (g) Persistence versus prominence scatter plot on logarithmic frequency scale. (h) Death time distribution. The embedded table summarizes key metrics with percent changes. At 10000 K, persistence distributions shift away from crystalline reference values, indicating a transition toward a more disordered structure.

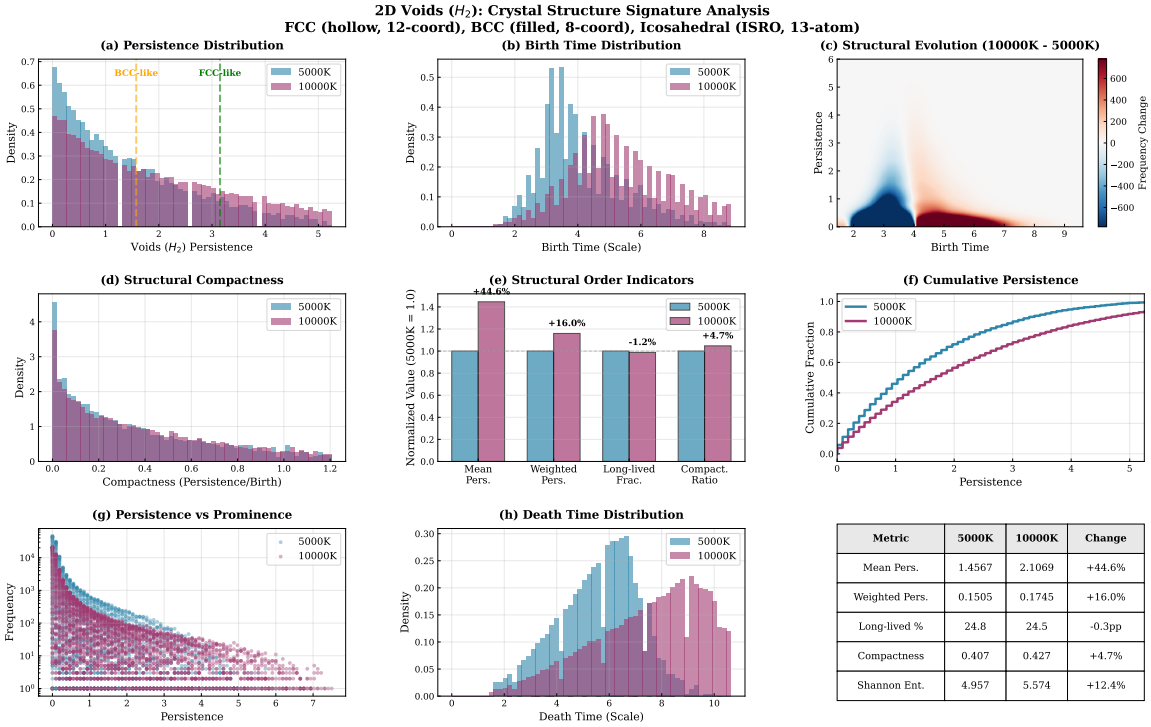

Figure 10. Topological signatures of H_2 features (2D voids) in liquid Cu at 5000 K and 10000 K in comparison with crystalline structure references. Panel organization follows Figure 9. (e) Structural order indicators showing mean persistence increase of +44.6%, weighted persistence +16.0%, long-lived fraction change of −0.3pp, compactness +4.7%, and Shannon entropy +12.4%. Void topology showing a more pronounced reorganization than holes, with birth and death time distributions broadening significantly at 10000 K, consistent with dissolution of stable cage structures and emergence of diverse void configurations above the Frenkel line.

Comparison with glass-forming systems provides additional context. Nakamura et al. [2015] showed that glassy SiO_2 displays characteristic curves in persistence diagrams reflecting directional Si-O-Si bonding constraints, with vertical profiles indicating narrow bond length distributions. The amorphous Si maintains sharp features corresponding to tetrahedral coordination, while the liquid Si above T_m shows broader persistence distributions similar to those of Cu above the FL, with profiles indicating dense random packing without characteristic motifs.

The supercritical liquid Cu below the FL shows the topological characteristics intermediate between crystalline metals (sharp, isolated features) and metallic glasses (moderately diffuse distributions). Above the FL, signatures shift toward high-temperature liquids with minimal medium-range order despite maintaining liquid-like density and coordination. As demonstrated by Onodera et al. [2019], network liquids show persistent, high-frequency features (stable networks) while molecular liquids show diverse, low-frequency features (weakly interacting units). Our Cu above the FL exhibits the latter without discrete molecular units, suggesting the FL involves a transition from network-like (cooperatively rearranging cages) to molecule-like (weakly correlated collision partners) correlations even in monatomic metallic liquids. This reinforces the interpretation of the FL as a genuine topological transition, not merely a dynamical crossover.

3.4 Integrated Analysis

A correlation between the topological and transport properties establishes the connection between reorganization and anomalies (Figure S8). TDA entropy (+14.2%) and persistence (+17.9%) correlate with the RDF peak shift (+35.3%) and diffusion increase (+184.6%), while coordination number (−20.0%) and viscosity (−8.8%) decrease.

4 Discussion

4.1 Physical Interpretation

Below the FL, atomic motion is dominated by liquid-like diffusion: oscillation around quasi-equilibrium positions before hopping to adjacent sites [Brazhkin et al., 2012a]. Persistent homology reflects this through stable H_1 loops representing medium-range cages with high total frequency (1.86×10^6) and relatively few but stable H_2 voids. Moderate Shannon entropy (5.07 for

H_1, 4.98 for H_2) indicates atoms constrained within characteristic cages.

At the FL (∼8000 K), the system exhibits maximum structural complexity. Viscosity reaches a minimum as the onset of gas-like ballistic motion (which would reduce viscosity through loss of cage constraints) is counterbalanced by increased momentum transfer through collisions. The RDF shows significant peaks, but persistent homology reveals that medium-range connectivity begins breaking down.

Above the FL (10000 K), a dramatic decrease in total frequency for H_1 (−15%) and H_2 (−23%) indicates dissolution of stable medium-range structures. However, a simultaneous increase in feature count (H_1: +125%, H_2: +119%) and weighted persistence (H_1: +18%, H_2: +20%) reveals that the structure does not become uniform. Instead, a wider variety of features emerge, occurring less frequently but persisting over longer length scales. This indicates a transition toward gas-like behavior where atoms move ballistically but still experience frequent collisions in a compressed environment.

Maintenance of relatively high coordination (CN ∼11) despite gas-like dynamics confirms that the structure is not a dilute gas. Instead, atoms are densely packed but lack a medium-range cage connectivity characteristic of liquids. The decrease of persistent medium-range cages enhances momentum transfer and shear resistance through collisional interactions, a phenomenon called "collisional viscosity enhancement."

The positive temperature coefficient above the FL is consistent with Enskog theory for dense fluids [Bell et al., 2021, Jervell et al., 2024]. Enskog theory decomposes shear viscosity into kinetic (η_{kk}, translational momentum transfer) and configurational (η_{cc}, collisional momentum transfer) contributions. In dilute gases, η_{kk} dominates and viscosity decreases with density. In dense supercritical fluids, η_{cc} becomes dominant. As temperature increases, the collision frequency and momentum exchange efficiency increase, enhancing the viscosity, which is opposite to the Arrhenius-like liquid behavior. Bell et al. [Bell et al., 2021] showed that the crossover ($\eta_{kk} = \eta_{cc}$) coincides with the kinematic viscosity minimum in supercritical fluids, analogous to our observations. Our persistent homology provides the first topological structural evidence for this collisional mechanism in metallic liquids, linking the breakdown of stable medium-range caging (decreased H_2 frequency) to emergence of dense, collision-dominated transport.

The Shannon entropy increase (+14.2% for H_1, +14.7% for H_2) quantifies the increased topological diversity and confirms that the supercritical fluid above the FL is structurally more heterogeneous than the liquid below the FL, despite appearances of "disorder" in conventional metrics.

4.2 Comparison with other systems

Our findings align with theoretical and computational studies showing anomalous transport near the FL [Brazhkin et al., 2012a,b, Bolmatov et al., 2014, Trachenko, 2023]. A loss of transverse phonon modes above the FL has been demonstrated in various systems; persistent homology provides complementary structural evidence for metallic liquids, directly quantifying the medium-range heterogeneity manifesting as anomalous transport.

The maintenance of high coordination above the FL has been noted but not fully explained structurally. Our analysis reveals that it reflects a genuine structural regime: atoms maintain many nearest neighbors (preserved short-range order) but medium-range connectivity characterized by loops (H_1) and cages (H_2) is fundamentally disrupted. Increased weighted persistence with decreased frequency indicates that the remaining features are larger but rare and transient rather than characteristic motifs.

The FL transition in dense metallic systems differs qualitatively from conventional gas-liquid transitions. Rather than the density decrease, the FL involves topological reorganization preserving short-range packing while losing medium-range connectivity.

The predicted viscosity minimum temperature $T_{\rm vm} \approx 7340$ K [Ojovan and Louzguine-Luzgin, 2024b] agrees well with our observed one: 8000 K, validating our identification and supporting the theoretical framework connecting the viscosity minima to the FL in supercritical metallic liquids [Ojovan and Louzguine-Luzgin, 2024b].

Table 5 presents melting and characteristic crossover temperatures for various metals. The table includes the melting temperature (T_m), glass transition temperature (T_g), the Arrhenius temperature (T_A), and the viscosity minimum temperature ($T_{\rm vm}$). These temperatures characterize distinct dynamical regimes in liquid metals, with $T_{\rm vm}$ corresponding to the Frenkel line location where the transition from liquid-like to gas-like dynamics occurs.

As shown in Table 5, the ratio $T_{\rm vm}/T_m$ varies systematically across different metals, with Cu exhibiting $T_{\rm vm}/T_m \approx 5.4$, consistent with the behavior of refractory metals. Our observed viscosity

Table 5. Melting (T_m) and crossover temperatures (T_g, T_A, $T_{\rm vm}$) for various metals. T_g is the glass transition temperature, T_A is the Arrhenius temperature marking the onset of simple activated flow, and $T_{\rm vm}$ is the theoretical viscosity minimum temperature predicted earlier. Data from Ref. [Ojovan and Louzguine-Luzgin, 2025].

Metal	T_m **(K)**	T_g **(K)**	T_A **(K)**	$T_{\rm vm}$ **(K)**
Hg	234	169	257	604
Na	370	189	407	1260
K	337	166	371	1210
Pb	600	—	660	2510
Bi	544	202	598	1550
Ga	303	97	333	920
Sn	505	159	556	1720
Cu	1358	794	1495	7340

minimum at 8000 K is in excellent agreement with the predicted value of 7340 K, falling within the expected range considering experimental uncertainties and the approximate nature of interatomic potentials at extreme conditions.

4.3 Further implications

The viscosity increase observed at high temperatures has significant implications for extreme environments. Industrial processes involve transient high-temperature excursions [DebRoy et al., 2018]. Our results indicate that the transport properties cannot be extrapolated from lower temperatures using the simple Arrhenius law [Angell, 1995] or power-law scaling [Mudry et al., 2013].

Geophysical applications are equally significant. Planetary cores exist at pressures and temperatures placing them in the supercritical regime [Anzellini et al., 2013]. Anomalous viscosity at high temperatures and pressures influences core dynamics indicating that thermal evolution models may need a revision [Laneuville et al., 2014].

Our demonstration that topological data analysis quantifies medium-range reorganization opens new avenues for understanding glass formation, crystallization kinetics, and phase separation in multicomponent alloys under extreme conditions [Louzguine-Luzgin et al., 2024, Sørensen et al., 2020].

Persistent homology and especially differential diagrams detect subtle medium-range order changes invisible to RDFs, with broad applicability to metallic and oxide liquids. Key advantages include: (i) multi-scale analysis capturing features from nearest-neighbor to collective medium-range structures; (ii) separate characterization of 1D loops and 2D voids providing comprehensive pictures; (iii) quantitative descriptors with bootstrap confidence intervals enabling objective comparison; and (iv) sensitivity to connectivity and geometry ideal for detecting transitions preserving short-range order while altering medium-range topology. This methodology extends to supercritical water, ionic liquids, metallic glasses [Cheng and Ma, 2011, Wang, 2012], and biomolecular assemblies where medium-range order is crucial but difficult to characterize by traditional methods.

4.4 Limitations

While our results provide compelling evidence for topological reorganization at the Frenkel line, several limitations should be acknowledged. First, our simulations rely on classical MD with an empirical potential (EAM), which may not fully capture the effects of electronic structure at very high temperatures. Ab initio MD simulations would provide a more accurate description of bonding changes but are computationally prohibitive for the system sizes and timescales required for converged topological analysis.

Second, the pressure dependence of the topological reorganization remains unexplored. Systematic studies varying both temperature and pressure would map out the FL in the full thermodynamic phase space and determine how topological signatures evolve along different paths through the supercritical region.

Finally, extension to multicomponent alloys would reveal how chemical ordering couples to topological reorganization. In particular, the interplay between phase separation [Louzguine-Luzgin et al., 2024] and FL crossing in binary and ternary metallic liquids remains an open question with significant implications for materials processing.

5 Conclusions

We demonstrated that liquid copper at 10 GPa exhibits anomalous temperature dependence of viscosity at high temperature, with viscosity increasing rather than decreasing above ∼8000 K. Combined MD simulation and topological data analysis revealed that this transport anomaly correlates with fundamental medium-range topological reorganization.

Key findings include: (i) viscosity minimum at 7000–8000 K with the diffusion slope kink and a statistically significant Stokes–Einstein breakdown ($D\eta/T$ reduced by 48% at 8000 K, non-overlapping confidence intervals at all above-FL temperatures) indicating a transport mechanism transition; (ii) dramatic topological reorganization with feature diversity increasing 119–125% while stability decreases 15–23%, indicating dissolution of characteristic cages and emergence of heterogeneous transient networks; (iii) Shannon entropy increases 14–15% with mean persistence increases 42–49%, confirmed by rigorous statistical tests ($p < 10^{-5}$); (iv) anomalous viscosity arises from transition from cooperative cage-based transport to collisional momentum transfer while maintaining liquid-like density, with topological evidence for this crossover; and (v) persistent homology provides powerful quantitative descriptors complementing traditional pair correlations, broadly applicable to understanding structural transitions under extreme conditions.

Our results establish the Frenkel line as a genuine structural and dynamical transition in supercritical metallic liquids, characterized by quantifiable topological reorganization underlying anomalous transport. These findings have implications for high-pressure materials processing, planetary core dynamics, and fundamental understanding of liquid structure and transport in extreme environments.

Acknowledgments

This work was supported in part by the Tohoku University-Tsinghua University Collaborative Research Fund 2025.

Data availability

The data cannot be made publicly available upon publication because no suitable repository exists for hosting data in this field of study. The data that support the findings of this study are available upon reasonable request from the authors.

References

C. Austen Angell. Formation of glasses from liquids and biopolymers. Science, 267(5206): 1924–1935, 1995.

L. D. Landau and E. M. Lifshitz. Statistical physics. Course of Theoretical Physics, 5, 1964.

Kostya Trachenko. Theory of liquids: From excitations to thermodynamics. Reports on Progress in Physics, 86(1):016501, 2023.

Michael I Ojovan and Dmitri V Louzguine-Luzgin. On crossover temperatures of viscous flow related to structural rearrangements in liquids. Materials, 17(6):1261, 2024a.

FH MacDougall. Kinetic theory of liquids. by j. frenkel. The Journal of Physical Chemistry, 51(4): 1032–1033, 1947.

G. G. Simeoni, T. Bryk, F. A. Gorelli, M. Krisch, G. Ruocco, M. Santoro, and T. Scopigno. The widom line as the crossover between liquid-like and gas-like behaviour in supercritical fluids. Nature Physics, 6(7):503–507, 2010.

Vadim V. Brazhkin, Yu D. Fomin, A. G. Lyapin, V. N. Ryzhov, and Kostya Trachenko. Two liquid states of matter: A dynamic line on a phase diagram. Physical Review E, 85(3):031203, 2012a.

V. V. Brazhkin, Yu D. Fomin, A. G. Lyapin, V. N. Ryzhov, E. N. Tsiok, and Kostya Trachenko. Where is the supercritical fluid on the phase diagram? Physics-Uspekhi, 55(11):1061, 2012b.

Dima Bolmatov, V. V. Brazhkin, and K. Trachenko. Thermodynamic behaviour of supercritical matter. Nature Communications, 4:2331, 2013.

Dima Bolmatov, Dmitry Zav'yalov, Mikhail Zhernenkov, Edvard T Musaev, and Yong Q Cai. Unified phonon-based approach to the thermodynamics of solid, liquid and gas states. Annals of Physics, 363:221–242, 2015.

Dima Bolmatov, D Zav'Yalov, M Gao, and Mikhail Zhernenkov. Structural evolution of supercritical co2 across the frenkel line. The journal of physical chemistry letters, 5(16): 2785–2790, 2014.

L. Larini, A. Ottochian, C. De Michele, and D. Leporini. Universal scaling between structural relaxation and vibrational dynamics in glass-forming liquids and polymers. Nature Physics, 4(1): 42–45, 2008.

Jean-François Wax and Eva Mocchetti. Simulation study of the collective excitations in liquid sodium under high pressure. Journal of Physics: Condensed Matter, 35(30):304003, 2023.

Michael I Ojovan and Dmitri V Louzguine-Luzgin. The minima of viscosities. Materials, 17(8): 1822, 2024b.

Dmitri V Louzguine-Luzgin, Larissa V Louzguina-Luzgina, and Hans Fecht. On limitations of the viscosity versus temperature plot for glass-forming substances. Materials Letters, 182:355–358, 2016.

Herbert Edelsbrunner and John L. Harer. Computational Topology: An Introduction. American Mathematical Society, 2010.

Gunnar Carlsson. Topology and data. Bulletin of the American Mathematical Society, 46(2): 255–308, 2009.

Steve Plimpton. Fast parallel algorithms for short-range molecular dynamics. Journal of Computational Physics, 117(1):1–19, 1995.

W. Michael Brown, Peng Wang, Steven J. Plimpton, and Allan N. Tharrington. Implementing molecular dynamics on hybrid high performance computers–short range forces. Computer Physics Communications, 182(4):898–911, 2011.

MI Mendelev and Alexander H King. The interactions of self-interstitials with twin boundaries. Philosophical Magazine, 93(10-12):1268–1278, 2013.

Said Bogtob, A Samiri, A Khmich, and A Hasnaoui. Effect of ni-reinforcement size on mechanical properties of al metallic glass matrix from molecular dynamics. Journal of Non-Crystalline Solids, 646:123211, 2024.

Shuichi Nosé. A unified formulation of the constant temperature molecular dynamics methods. The Journal of Chemical Physics, 81(1):511–519, 1984.

William G. Hoover. Canonical dynamics: Equilibrium phase-space distributions. Physical Review A, 31(3):1695, 1985.

Herman JC Berendsen, JPM van Postma, Wilfred F. van Gunsteren, ARHJ DiNola, and Jan R. Haak. Molecular dynamics with coupling to an external bath. The Journal of Chemical Physics, 81(8):3684–3690, 1984.

Glenn J. Martyna, Douglas J. Tobias, and Michael L. Klein. Constant pressure molecular dynamics algorithms. The Journal of Chemical Physics, 101(5):4177–4189, 1994.

V. E. Zinoviev. Thermophysical properties of metals at high temperatures. Metallurgiya, Moscow, 1989.

MM Demin, ON Koroleva, AV Shapranov, and AA Aleksashkina. Atomistic modeling of the critical region of copper using a liquid-vapor coexistence curve. Mathematica Montisnigri, 46, 2019.

Melville S. Green. Markoff random processes and the statistical mechanics of time-dependent phenomena. ii. irreversible processes in fluids. The Journal of Chemical Physics, 22(3):398–413, 1954.

Ryogo Kubo. Statistical-mechanical theory of irreversible processes. i. general theory and simple applications to magnetic and conduction problems. Journal of the Physical Society of Japan, 12 (6):570–586, 1957.

Herbert Edelsbrunner and Ernst P. Mücke. Three-dimensional alpha shapes. ACM Transactions on Graphics (TOG), 13(1):43–72, 1994.

Ippei Obayashi, Takenobu Nakamura, and Yasuaki Hiraoka. Persistent homology analysis for materials research and persistent homology software: Homcloud. Journal of the Physical Society of Japan, 91(9):091013, 2022. doi: 10.7566/JPSJ.91.091013.

Takenobu Nakamura, Yasuaki Hiraoka, Akihiko Hirata, Emerson G. Escolar, and Yasumasa Nishiura. Persistent homology and many-body atomic structure for medium-range order in the glass. Nanotechnology, 26(30):304001, 2015. doi: 10.1088/0957-4484/26/30/304001.

Mickaël Buchet, Yasuaki Hiraoka, and Ippei Obayashi. Persistent homology and materials informatics. In Isao Tanaka, editor, Nanoinformatics, pages 75–95. Springer, Singapore, 2016. doi: 10.1007/978-981-10-7617-6_5.

William F. Gale and Terry C. Totemeier. Smithells metals reference book. Elsevier, 8th edition, 2004.

M. J. Assael, K. Kakosimos, R. M. Banish, J. Brillo, I. Egry, R. Brooks, P. N. Quested, K. C. Mills, A. Nagashima, Y. Sato, et al. Reference data for the density and viscosity of liquid copper and liquid tin. Journal of Physical and Chemical Reference Data, 39(3):033105, 2010.

J. A. Cahill and A. D. Kirshenbaum. High-temperature properties of liquid copper. The Journal of Physical Chemistry, 66(6):1080–1082, 1962.

Mikhail Mikhailovich Demin, Olga Nikolaevna Koroleva, Anna Andreevna Aleksashkina, and Vladimir Ivanovich Mazhukin. Molecular-dynamic modeling of thermophysical properties of phonon subsystem of copper in wide temperature range. Mathematica Montisnigri, 47, 2020.

Y. Mishin, M. J. Mehl, D. A. Papaconstantopoulos, A. F. Voter, and J. D. Kress. Structural stability and lattice defects in copper: Ab initio, tight-binding, and embedded-atom calculations. Physical Review B, 63(22):224106, 2001.

C Chang, HP Zhang, R Zhao, FC Li, P Luo, MZ Li, and HY Bai. Liquid-like atoms in dense-packed solid glasses. Nature Materials, 21(11):1240–1245, 2022.

Yohei Onodera, Shinji Kohara, Shuta Tahara, Atsunobu Masuno, Hiroyuki Inoue, Motoki Shiga, Akihiko Hirata, Koichi Tsuchiya, Yasuaki Hiraoka, Ippei Obayashi, Koji Ohara, Akitoshi Mizuno, and Osami Sakata. Understanding diffraction patterns of glassy, liquid and amorphous materials via persistent homology analyses. Journal of the Ceramic Society of Japan, 127(12): 853–863, 2019. doi: 10.2109/jcersj2.19143.

Ian H Bell, Stephanie Delage-Santacreu, Hai Hoang, and Guillaume Galliero. Dynamic crossover in fluids: From hard spheres to molecules. The Journal of Physical Chemistry Letters, 12(27): 6411–6417, 2021.

Vegard G. Jervell, Even Solbraa Bjørn, Øivind Wilhelmsen, Morten Hammer, and Åsmund Ervik. Predicting viscosities and thermal conductivities from dilute gas to dense liquid. Journal of Chemical Physics, 161(23):234106, 2024. doi: 10.1063/5.0236883.

Michael I Ojovan and Dmitri V Louzguine-Luzgin. Three crossover temperatures related to structural changes in glass forming systems. Physics and Chemistry of Glasses-European Journal of Glass Science and Technology Part B, 66(6):273–274, 2025.

T. DebRoy, H. L. Wei, J. S. Zuback, T. Mukherjee, J. W. Elmer, J. O. Milewski, A. M. Beese, A. Wilson-Heid, A. De, and W. Zhang. Additive manufacturing of metallic components–process, structure and properties. Progress in Materials Science, 92:112–224, 2018.

Stepan Mudry, Andriy Korolyshyn, Volodymyr Vus, and Andriy Yakymovych. Viscosity and structure of liquid cu–in alloys. Journal of Molecular Liquids, 179:94–97, 2013.

Simone Anzellini, Agnès Dewaele, Mohamed Mezouar, Paul Loubeyre, and Guillaume Morard. Melting of iron at earth's inner core boundary based on fast x-ray diffraction. Science, 340(6131): 464–466, 2013.

M Laneuville, MA Wieczorek, D Breuer, J Aubert, G Morard, and Tina Rückriemen. A long-lived lunar dynamo powered by core crystallization. Earth and Planetary Science Letters, 401: 251–260, 2014.

DV Louzguine-Luzgin, RV Belosludov, and MI Ojovan. Room-temperature pressure-induced phase separation in glassy alloys. Materials Today Communications, 40:109453, 2024.

Søren S Sørensen, Christophe AN Biscio, Mathieu Bauchy, Lisbeth Fajstrup, and Morten M Smedskjaer. Revealing hidden medium-range order in amorphous materials using topological data analysis. Science Advances, 6(37):eabc2320, 2020.

Y. Q. Cheng and E. Ma. Atomic-level structure and structure–property relationship in metallic glasses. Progress in Materials Science, 56(4):379–473, 2011.

Wei Hua Wang. The elastic properties, elastic models and elastic perspectives of metallic glasses. Progress in Materials Science, 57(3):487–656, 2012.